Materials Today Bio 26 (2024) 101037

Contents lists available at ScienceDirect

Materials Today Bio

journal homepage: www.journals.elsevier.com/materials-today-bio

A dual-targeting therapeutic nanobubble for imaging-guided atherosclerosis treatment

Jie Lin [a,1], Xiaoying Chen [a,1], Yi Li [a], Luodan Yu [d,**], Yu Chen [c,e,*], Bo Zhang [a,b,***]

[a] Department of Ultrasound, Shanghai East Hospital, Tongji University School of Medicine, Shanghai, 200120, PR China
[b] State Key Laboratory of Cardiology and Medical Innovation Center, Shanghai East Hospital, School of Medicine, Tongji University, Shanghai, 200120, PR China
[c] Materdicine Lab, School of Life Sciences, Shanghai University, Shanghai, 200444, PR China
[d] Department of Radiology, Shanghai Institute of Thoracic Oncology, Shanghai Chest Hospital, Shanghai Jiao Tong University School of Medicine, Shanghai, 200030, PR China
[e] Shanghai Institute of Materdicine, Shanghai, 200051, PR China

ARTICLE INFO

Keywords:
Nanobubbles
Low shear stress
Inflammatory
Atherosclerosis
Ultrasound

ABSTRACT

Atherosclerosis is a cardiovascular disease that seriously endangers human health. Low shear stress (LSS) is recognized as a vital factor in causing chronic inflammatory and further inducing the occurrence and development of atherosclerosis. Targeting imaging and treatment are of substantial significance for the diagnosis and therapy of atherosclerosis. On this ground, a kind of ultrasound (US) imaging-guided therapeutic polymer nanobubbles (NBs) with dual targeting of magnetism and antibody was rationally designed and constructed for the efficiently treating LSS-mediated atherosclerosis. Under the combined targeting effect of an external magnetic field and antibodies, the drug-loaded therapeutic NBs can be effectively accumulated in the inflammatory area caused by LSS. Upon US irradiation, the NBs can be selectively disrupted, leading to the rapid release of the loaded drugs at the targeted site. Notably, the US irradiation generates a cavitation effect that induces repairable micro gaps in nearby cells, thereby enhancing the uptake of released drugs and further improving the therapeutic effect. The prominent US imaging, efficient anti-inflammatory effect and treatment outcome of LSS-mediated atherosclerosis had been verified *in vivo* on a surgically constructed LSS-atherosclerosis animal model. This work showcased the potential of the designed NBs with multifunctionality for *in vivo* imaging, dual-targeting, and drug delivery in the treatment of atherosclerosis.

1. Introduction

Atherosclerosis is a chronic inflammatory disease that can lead to various cardiovascular diseases and further induce acute heart events, stroke or other severe clinical outcomes [1,2]. Nowadays, a range of medications have been used on anti-atherosclerosis including lipid-lowering medicines, hypotensive drugs, anti-thrombotic and anti-platelet drugs. Despite these treatments, the incidence and mortality associated with cardiovascular diseases caused by atherosclerosis remain high. Therefore, early-stage diagnosis and intervention are crucial in reducing the prevalence of these cardiovascular diseases and saving patients' lives.

Understanding the basic pathogenesis of atherosclerosis is the foundation for seeking effective treatment methods. Several theories have been proposed to explain its pathogenesis, including lipid infiltration, inflammation, oxidative stress, and endothelial injury-response theories [3]. Medical imaging and pathology show that atherosclerosis plaques are commonly found in areas with abnormal hemodynamics, such as vascular bifurcations and bends [4]. Thus, the hemodynamic genesis theory offers a new perspective for understanding

* Corresponding author. Materdicine Lab, School of Life Sciences, Shanghai University, Shanghai, 200444, PR China.
** Corresponding author. Department of Radiology, Shanghai Institute of Throacic Oncology, Shanghai Chest Hospital, Shanghai Jiao Tong University School of Medicine, Shanghai, 200030, PR China.
*** Corresponding author. Department of Ultrasound, Shanghai East Hospital, Tongji University School of Medicine, Shanghai, 200120, PR China.
E-mail addresses: yuluodan@yeah.net (L. Yu), chenyuedu@shu.edu.cn (Y. Chen), zhangbo2016@tongji.edu.cn (B. Zhang).
[1] Jie Lin and Xiaoying Chen contributed to this work equally.

https://doi.org/10.1016/j.mtbio.2024.101037
Received 21 December 2023; Received in revised form 5 March 2024; Accepted 19 March 2024
Available online 22 March 2024

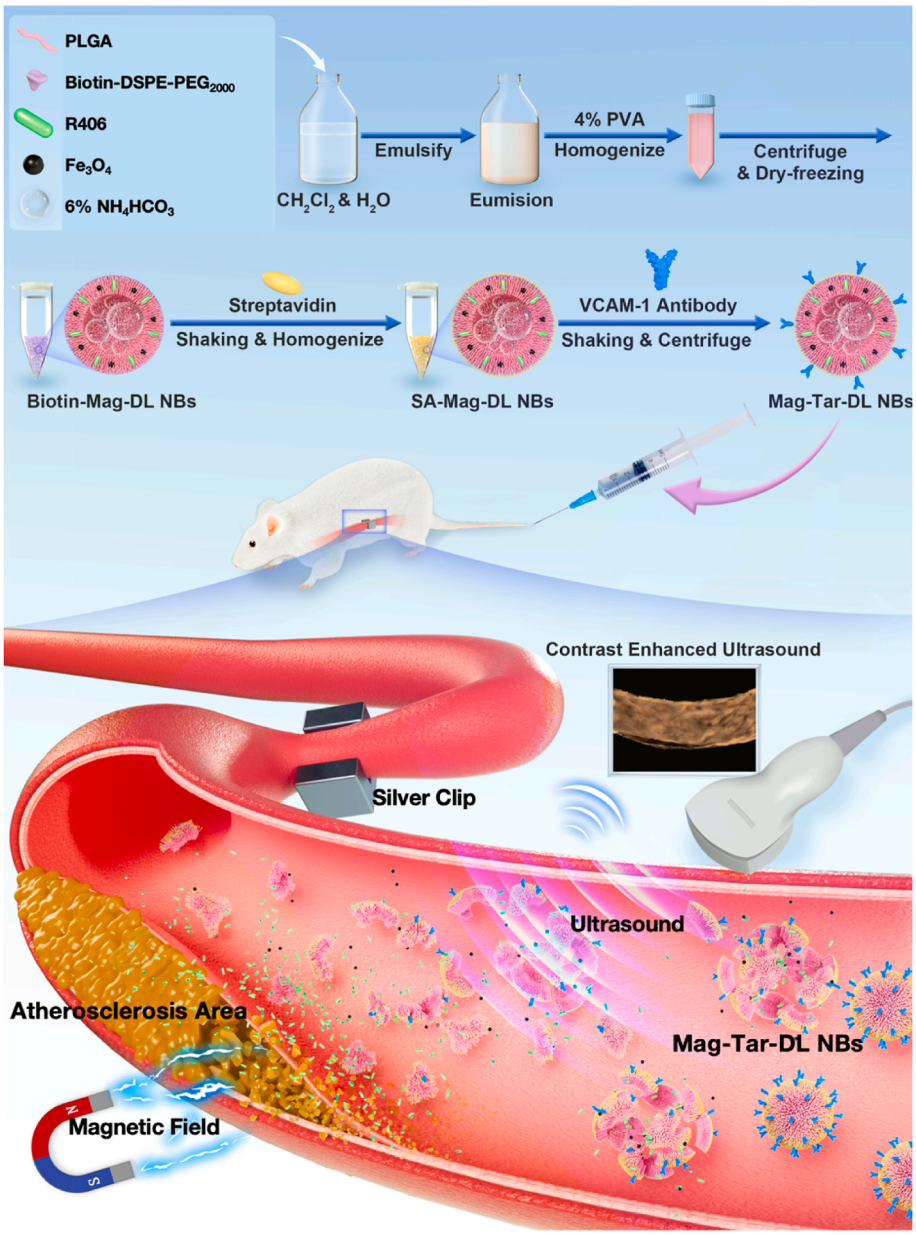

Fig. 1. Schematic diagram of the synthetic process of Mag-Tar-DL NBs and their underlying mechanism in the treatment of LSS-mediated atherosclerosis (Biotin-Mag-DL NBs: Biotinylated magnetic drug-loaded NBs; SA-Mag-DL NBs: Streptavidin-magnetic drug-loaded NBs; Mag-Tar-DL NBs: magnetic-antibody dual-targeting drug-loaded NBs; Tar-DL NBs: antibody targeting drug-loaded NBs; DL NBs: drug-loaded NBs).

atherosclerosis. Wall shear stress (WSS) is a tangential force exerted by flowing blood on the vessel wall, and the theory suggests that persistently low shear stress (LSS) may be a crucial factor in causing local chronic inflammation in the vascular, potentially leading to the development of atherosclerotic plaques [5,6].

Relevant research has shown that LSS acts as a mechanical stimulus on endothelial cells, leading to the upregulation of platelet endothelial cell adhesion factor (PECAM-1). This, in turn, activates the nuclear factor-κ-gene binding (NF-κB) pathway, causing the release of various chemokines and adhesion factors. Vascular cell adhesion molecule-1 (VCAM-1), also known as CD106, is a crucial adhesion molecule primarily expressed on the surface of activated endothelial cells. It has a significant presence in atherosclerotic conditions, facilitating the adhesion and transmigration of white blood cells. Additionally, VCAM-1 can be secreted into the bloodstream, potentially initiating a wider range of inflammatory responses [7]. These factors contribute to local endothelial inflammation and abnormal intima thickening, eventually leading to arterial inflammation and the advancement of atherosclerosis [8–10]. Phosphorylation of spleen tyrosine kinase (SYK) is pivotal in this inflammation-related signaling pathway [11–13]. Studies indicate that SYK inhibitor, such as R406, can markedly curb the inflammatory response throughout the body [14,15] and may impede the progression of atherosclerosis. R406 has been shown to prevent the phosphorylation of SYK and block the subsequent activation of inflammasomes, reducing inflammation. Research has revealed that R406 effectively combats inflammatory diseases, including arthritis and retinitis [14,15]. Consequently, it is plausible to anticipate that R406, as an anti-inflammatory agent, could inhibit the early stages of atherosclerosis.

Although ultrasonic imaging is the main diagnostic technique and has shown positive effects in diagnosing atherosclerosis, it gets difficulties in detecting plaques during the early stages of the disease [16]. The emergence of microbubble contrast agents has improved the sensitivity and resolution of US imaging, making it a desirable technique for disease diagnosis [17–19]. Moreover, microbubbles also serve as

efficient drug delivery vehicles [20–22]. However, the large particle size of microbubbles significantly limits their therapeutic efficacy, necessitating the development of smaller-sized bubbles, such as nanobubbles (NBs). Additionally, the continuous high-shear stress of blood flow in arteries makes it difficult for conventional NBs to adhere to blood vessels in the target area. Consequently, there is an urgent need to develop active-targeting therapeutic NBs for efficient US imaging and anti-atherosclerosis therapy in the early stages of the disease.

In this study, we constructed a dual-targeting drug delivery system that combines magnetic and antibody targeting for imaging-guided anti-atherosclerosis therapy. PLGA (poly (lactic-*co*-glycolic acid)), Biotin-DSPE-PEG_{2000}, R406, Fe_3O_4, and Biotin-VCAM-1 were used to construct dual-targeting drug-loaded polymer NBs with the double emulsification method and the biotin-avidin bridging approach. Specifically, Fe_3O_4 imparted magnetism to the NBs, while the VCAM-1 antibody provided antibody targeting. Through the dual effects of an external magnetic field and the targeting antibody, the drug-loaded NBs (DL NBs) can preferentially accumulate in areas of vascular inflammation. Under US irradiation, the designed NBs could be disrupted to release the loaded R406 *in situ*, inhibiting the inflammatory response in the targeted area and thus preventing the progression of atherosclerosis. Notably, the enhanced US imaging facilitated the detection of atherosclerotic plaques more effectively by using NBs as contrast agents. In this study, surgery was performed to place silver clips on the abdominal aorta of C57 mice to establish the low shear stress (LSS) model. The US imager was utilized to monitor the regional blood vessels before and after model induction (Fig. 1). These contents of imaging detection involved measuring blood flow velocity, analyzing shear stress, and assessing the accumulation of magnetic-antibody dual-targeting drug-loaded NBs (Mag-Tar-DL NBs) in the LSS region. After two weeks of treatment, arterial tissue from the LSS area was harvested, and both H&E and immunohistochemistry (IHC) staining for various inflammatory mediators were performed. By evaluating the expression of these mediators, we confirmed the therapeutic efficacy of the Mag-Tar-DL NBs *in vivo*.

2. Materials and methods

2.1. Cell line

RAW264.7 and human umbilical vein endothelial cells (HUVEC) were obtained from American type culture collection (ATCC). RAW264.7 cells were cultured in high sugar Dulbecco's modified eagle medium (DMEM) supplemented with 10% fetal bovine serum and 1% pen strep (100 U/mL penicillin and 100 μg/mL streptomycin). HUVEC cells were cultured in endothelial cell culture medium (ECM), supplemented with 10% fetal bovine serum, 1% pen strep and 1% growth factor. Trypsin-EDTA and PBS was purchased from Basal Media Technologies Co., Ltd. (Shanghai, China).

2.2. Materials and chemicals

PLGA (50:50; Mw = 30000) was purchased from Daigang Biomaterial Co., Ltd. (Jinan, China). dichloromethane and dimethyl sulfoxide (DMSO) were purchased from Titan Technology Company Co., Ltd. (Shanghai, China). Ammonium bicarbonate and polyvinyl alcohol (PVA) were purchased from Aladdin Chemistry Co., Ltd. (Shanghai, China). Fe_3O_4 Nanoparticles were purchased from Dongna Biological Company Co., Ltd. (Nanjing, China). Bio-DSPE-PEG_{2000} was purchased from Meiluo Biological Company Co., Ltd. (Shanghai, China). R406 (freebase) was purchased from MedChemexpress Co., Ltd. (New Jersey, USA). Cell counting kit-8 (CCK-8) reagent was purchased from Qihai Biological Co., Ltd. (Shanghai, China). Enzyme linked immunosorbent assay (ELISA) kits were purchased from Lianke biotech Co., Ltd. (Hangzhou, China). Dil, Hoechst 33342 and horseradish peroxidase labeled streptavidin (HRP-SA) were purchased from Beyotime Biotechnology Co., Ltd. (Shanghai, China). Agarose powder was purchased from Runcheng Biological Co., Ltd. (Shanghai, China).

2.3. Synthesis of Mag-Tar-DL NBs

Biotin-Mag-DL NBs were prepared by double emulsion method and then VCAM-1 antibody was connected to the surface of Biotin-Mag-DL NBs by biotin-avidin bridging method to obtain Mag-Tar-DL NBs. Specifically, 44 mg PLGA, 2 mg Biotin-DSPE-PEG_{2000}, 2 mg Fe_3O_4 nanoparticles and 2 mg R406 were co-dissolved in 2 mL dichloromethane. The mixture was allowed to stand at room temperature for 1 h until fully dissolved, and 200 μL 6% bicarbonate aqueous solution was added to the oily mixture. The mixture was emulsified 2 min by ultrasonic cell pulverizer under the conditions of 60 W, ice bath and pulse mode (3 s work, 3 s stop) to obtain the primary emulsion (O/W). The primary emulsion was transferred to 5 mL of 4% PVA and be homogenized at a speed of 20,000 rpm for 5 min to obtain the secondary emulsion (W/O/W). The secondary emulsion was transferred to 10 mL of ultrapure water and stirred magnetically at room temperature for 4–6 h to allow for the volatilization of the organic solvent. After volatilization, the NBs were collected by centrifugation at 2500 *g* for 5 min and then resuspend in ultrapure water for 3 times. Finally, the NBs were dispersed in 1 mL of ultrapure water, placed it in a refrigerator at −80 °C for 1 h, and then transferred to a vacuum freeze dryer for overnight freezing and drying. This process resulted in the formation of biotin-Mag-DL NBs.

To further endow the NBs with antibody-targeting ability, the prepared biotin-Mag-DL NBs were dispersed in ultrapure water. Streptavidin (SA) (5 μg/mL) was added to the solution, and the mixture was incubated on a shaker at 200 rpm and room temperature for 30 min. Centrifugation was used to remove unbound SA, and the precipitate was dispersed in ultrapure water. Biotinylated VCAM-1 antibody was then added to co-incubate with SA-Mag-DL NBs on a shaker (200 rpm, 30 min, and room temperature). After incubation, centrifugation was used to remove the unbound antibodies, and the Mag-Tar-DL NBs dispersion liquid was prepared with saline.

2.4. Drug encapsulation efficiency

Kurniawan et al. demonstrated that different concentrations of R406 showed absorption peak heights proportional to the concentration on high performance liquid chromatography (HPLC) [23]. We observed similar results on ultraviolet–visible (UV–Vis) spectroscopy, and therefore, UV–Vis spectroscopy was used to determine the content of R406 in NBs. To calculate the encapsulation rate of R406, R406 solutions with concentrations of 6.25 μg/mL, 12.5 μg/mL and 25 μg/mL was prepared by dissolving R406 in DMSO. UV–Vis spectroscopy was obtained to measure the absorbance of these R406 solutions. The absorbance curve of R406 in a certain wavelength range was observed, and the absorbance at 280 nm was selected to draw a fitting curve of the linear relationship between R406 concentration and absorption peak.

To determine the content of R406 in the sample, 0.8 mg of the R406-encapsulated NBs freeze-dried powder was dissolved in 4 mL DMSO, and the UV–Vis spectroscopy was obtained. Therefore, the absorbance at 280 nm of the sample was then compared to the fitting curve of linear relationship between R406 concentration and 280 nm absorption peak to confirm the content of R406. Finally, the encapsulation of the R406 was calculated according to encapsulation percentage (EN%) formula. The expression is EN% = Cb/Cs × 100%, where Cs is the total amount of drug added during synthesis, and Cb is the actual amount of drug in the designed NBs.

2.5. In vitro ultrasonic imaging

To conduct *in vitro* ultrasonic imaging, 3 mg of agar powder was dissolved in 200 mL of ultrapure water and heated with magnetic stirring to form an agarose colloid. This hot agarose solution was then poured into a mold to create a hollow agarose gel phantom. Mag-Tar-DL

NBs were dispersed in ultrapure water to prepare a gradient concentration dispersion liquid, and the concentration of this NBs dispersion liquid decreased exponentially. This dispersion liquid was added into the phantom's hole. The US imaging device was utilized to observe the NBs dispersion liquid within the pores on the phantom's side. The placement of the phantom, NBs, and probe is depicted in Fig. 3C. Both B-mode and contrast-enhanced imaging modes were employed for US imaging. Following this, the US imaging analyzer was used to analyze the NBs dispersion liquid's ultrasound contrast intensity in the region of interest.

2.6. Ultrasonic blasting and enhancement of drug release under US irradiation

Ultrasonic blasting of NBs under US is critical to rapidly release the loaded R406 in targeted tissues. To evaluate this, the acoustic imaging capabilities of the NBs before and after high intensity US irradiation were compared. The 1 mg/mL NBs dispersion liquid was added to the hollow hole of the agarose gel phantom, and the contrast mode was used to assess its acoustic imaging properties. Subsequently, the NBs were irradiated using an ultrasonic therapy instrument with the following conditions: 1 W/cm^2, 1 MHz, 50% duty cycle, and 1 min. After irradiation, the acoustic imaging capabilities of the NBs dispersion liquid within the agarose gel phantom were measured again by the ultrasonic imager. The imaging capabilities of the NBs within the phantom before and after high intensity US irradiation were compared to assess the ultrasonic blasting capability.

The ultraviolet absorption spectrum of different concentrations of R406 in PBS solution was detected with UV–Vis spectroscopy. R406-loaded Mag-Tar-DL NBs were resuspended in PBS to achieve a concentration of 50 μg/mL, containing 1.933 μg/mL R406. A 12-well plate was prepared with 1 mL of the above solution in each well, divided into a control group and an US irradiation group. The US irradiation group was exposed to US (0.72 W/cm^2, 1 MHz, 50% duty cycle, 1 min) at 0 h, 3 h, 6 h, and 12 h. At the beginning of the experiment, all the dispersion liquid in the wells from both groups was centrifuged (5500 rpm, 1 min), and the supernatant was analyzed by UV–Vis spectroscopy to calculate the starting concentration of R406 using the fitting curve. Subsequently, at 3 h, 6 h, 12 h, 24 h, and 48 h after the start of the experiment, the supernatant was again measured with UV–Vis spectroscopy.

2.7. Cell cytotoxicity evaluation

To evaluate the cytotoxicity of the designed NBs, RAW264.7 and HUVEC cells were plated in 96-well plates at a density of 1.0×10^4 and cultured overnight. Different concentrations of R406 solutions and Mag-Tar-DL NBs dispersion liquid were prepared with fresh medium. RAW264.7 and HUVEC cells were incubated with different concentrations of R406 solution (0.25, 0.5, 1.0 and 2.0 μg/mL) and Mag-Tar-DL NBs dispersion liquid (25, 50, 100, 200 μg/mL) for 24 h and 48 h. After the incubation, CCK-8 reagent was used for cell viability determination at two time points. The survival rate of untreated control group cells was 100%. Four replicates were repeated for each experiment group.

2.8. The anti-inflammation effect of R406

RAW264.7 and HUVEC cells (cell density: 2×10^5 cells/well and 2×10^4 cells/well) were plated in 24-well plates overnight and then treated by R406 at different concentrations (0, 0.5, 1.0, 1.5 μg/mL) and Lipopolysaccharide (LPS) (50 ng/mL) for 24 h. After incubation, the supernatant from RAW264.7 cells was collected for ELISA to measure tumor necrosis factor α (TNF-α), monocyte chemoattractant protein-1 (MCP-1) (chemokine ligand 2 (CCL-2)), and interleukin-6 (IL-6), while the supernatant from HUVEC cells was collected for ELISA to measure TNF-α, VCAM-1, and intercellular cell adhesion molecule-1 (ICAM-1). The impact of R406 concentration on the secretion of inflammatory factors in both RAW264.7 and HUVEC cells was investigated. Three replicates were repeated for each group of experiments.

2.9. The anti-inflammation effect of the designed NBs

RAW264.7 and HUVEC cells (cell density: 2×10^5 cells/well and 2×10^4 cells/well) were plated in 24-well plates overnight. After adding LPS to the cells to cause inflammation, RAW264.7 and HUVEC were separately incubated with 1.0 μg/mL R406, DL NBs of the same dose R406 and simple NBs for 24 h. After the incubation, the cell supernatant was collected. The supernatant of the RAW264.7 cell line was subjected to the ELISA experiment of TNF-α, MCP-1 (CCL-2) and IL-6, and the HUVEC cell line was subjected to the ELISA experiment of TNF-α, VCAM-1 and ICAM-1. Three replicates were repeated for each experiment group.

2.10. Effect of US on endothelial cell activity

The HUVEC cells were plated in a 24-well plate at a density of 1×10^4 cells/well and cultured overnight. The power of the ultrasonic therapy instrument (0.5–2.0 W/cm^2, 1 MHz, 50% duty cycle, 1 min) was adjusted, and the cells were irradiated from the bottom of the cell culture plate. After US irradiation, HUVEC cells were cultured for 3 h. CCK-8 experiment and calcein staining were performed to detect cell viability. Four replicates were repeated for each experiment group.

2.11. US enhanced the therapeutic effect of drugs

To verify that US could enhance the anti-inflammatory effect of drugs, HUVEC were implanted in a 12-well plate (cell density: 2×10^5 cells/well) and cultured overnight. They were divided into 3 groups (control group, R406 group and R406+US group) and LPS was used to stimulate the HUVEC into an inflammation reaction. In control group, the only 100 ng/mL LPS was added into culture medium. In R406 group, the 100 ng/mL LPS and 1.0 μg/mL R406 were added in culture medium. In the R406+US group, after addition of 100 ng/mL LPS and 1.0 μg/mL R406 to the culture medium, HUVEC were irradiated from the bottom of the culture dish using a US therapy device at a power of 0.72 W/cm^2 for 1 min. After treatment, HUVEC from all three groups were incubated in a constant temperature incubator for 24 h, after which the cell supernatants were collected for ELISA test to detect the expression of MCP-1 (CCL-2) and analyze the effect of US irradiation on the drug's therapeutic effect. Four replicates were repeated for each experiment group.

2.12. Evaluation of adhesion effect of NBs in vitro

To evaluate the antibody-targeting ability of the designed NBs, HUVEC cells were plated at a density of 1×10^4 cells/well in a 6-well plate and cultured overnight. HUVEC cells were then pretreated with 100 ng/mL LPS to induce an inflammatory state, and Dil was used to label the NBs. Subsequently, the inflammatory HUVEC cells were incubated with the labeled NBs, with or without antibody targeting, at the same concentration for 5 min. Following incubation, unbound NBs were removed with PBS washes, and the cells were stained with Hoechst 33342 (0.1%) for 10 min. After staining, excess dye was removed with PBS, and the cells were fixed with a tissue fixative. The adhesion ability of both targeted and non-targeted NBs to the inflammatory cells was observed under a fluorescence microscope.

2.13. US imaging of Mag-Tar-DL NBs in vivo

To perform US imaging, the mouse model was anesthetized with 1% sodium pentobarbital at a dose of 75 mg/kg. DL NBs, Tar-DL NBs, and Mag-Tar-DL NBs at a concentration of 0.5 mg/mL were injected into the mice *via* the tail vein. Subsequently, the low shear stress (LSS) region of

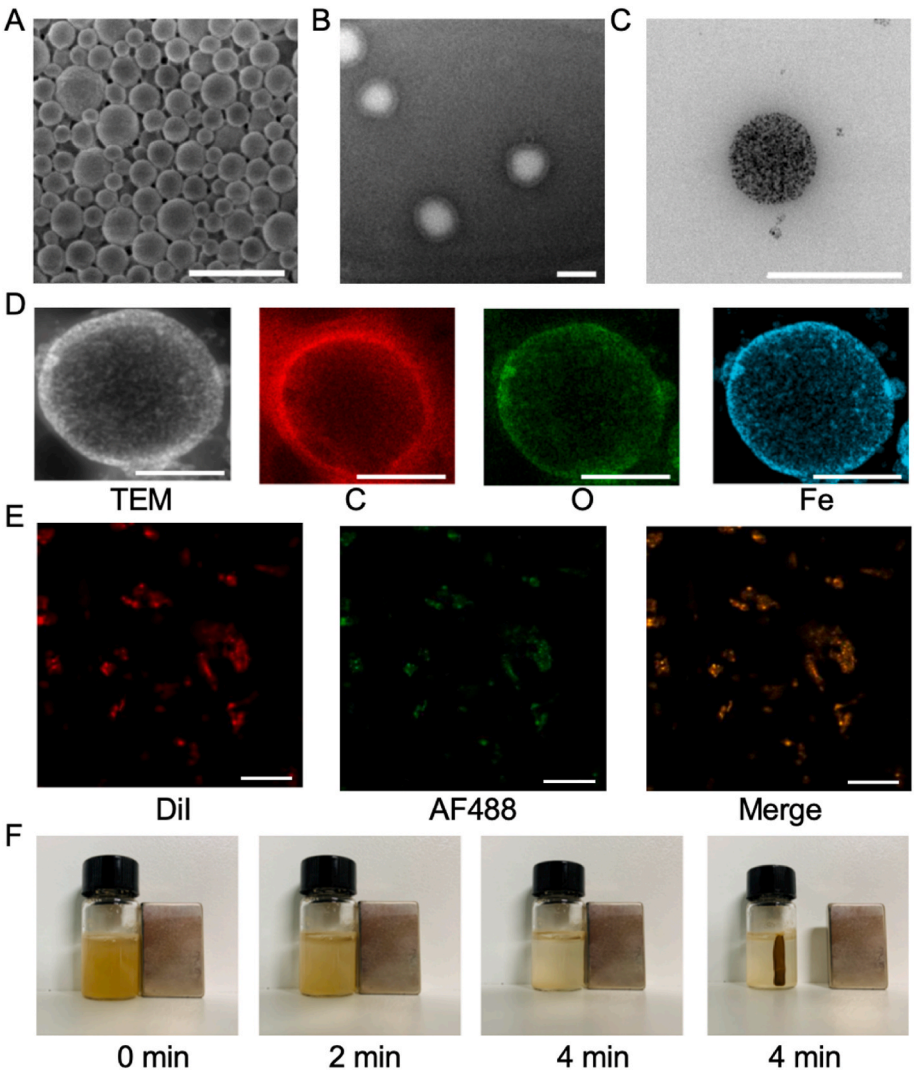

Fig. 2. Synthesis and characterizations of Mag-Tar-DL NBs. (A) SEM image, (B, C) TEM images and (D) EDS mapping of Mag-Tar-DL NBs. (Scale bar = 500 nm) (E) CLSM images of Mag-Tar-DL NBs (Scale bar = 50 μm). (F) Mag-Tar-DL NBs under the interventions of an applied magnet for prolonged durations (0, 2, and 4 min).

the mouse's abdominal aorta was imaged using an US imager before injection, 1- and 3-min post-injection. The adhesion of Mag-Tar-DL NBs to the LSS region was evaluated by analyzing the ultrasound contrast intensity.

2.14. The therapeutic effect evaluation of Mag-Tar-DL NBs in vivo

To evaluate the therapeutic efficacy of Mag-Tar-DL NBs, thirty healthy C57 mice were used to create LSS models and divided randomly into: (1) Control group; (2) US group; (3) R406 group; (4) Tar-DL NBs + US group; (5) Mag-Tar-DL NBs + US group randomly (n = 6). In the Control group, the same volume of saline as the other groups was injected during each treatment process without US irradiation. In the US group, an equal amount of saline was injected during each treatment process, and US was used to irradiate the mouse abdomen for 1 min at a power density of 1 W/cm^2. In the R406 group, 5 mg/kg R406 diluted in saline was injected each time without US irradiation. In the Tar-DL NBs + US group, the Tar-DL NBs equivalent to 5 mg/kg R406 dose were injected each time. After injection, the mouse's abdomen was irradiated by US therapy device for 1 min with the power density of 1 W/cm^2. In the Mag Tar DL NBs + US group, the Mag-Tar DL NBs equivalent to 5 mg/kg R406 dose were injected each time. After injection, the mouse's abdomen was also irradiated by US therapy device for 1 min with the power density of 1 W/cm^2. After 12 consecutive days of different treatments, the mice were sacrificed, and the abdominal aortas were taken out. The LSS areas of blood vessels were taken to make continuous paraffin sections. H&E staining was performed to observe the general condition of blood vessels. IHC staining were performed to analyze the expression of inflammatory factors in the LSS area after treatment. The detection indicators included VCAM-1, TNF-α and IL6.

2.15. Statistical analysis

All values given are mean ± SD. GraphPad Prism 7.0 (GraphPad Software, CA, USA) was used for statistical analysis. One-way analysis of variance was used to determine statistical differences between multiple groups. The *t*-test of unpaired students was used to analyze differences betwen two independent samples with equal variance. * is $P < 0.05$, ** is $P < 0.01$, *** is $P < 0.001$, **** is $P < 0.0001$.

3. Results

3.1. Construction and characterization of Mag-Tar-DL NBs

The double emulsification method is currently one of common methods to construct nano-scale bubbles (NBs) [24]. This method for

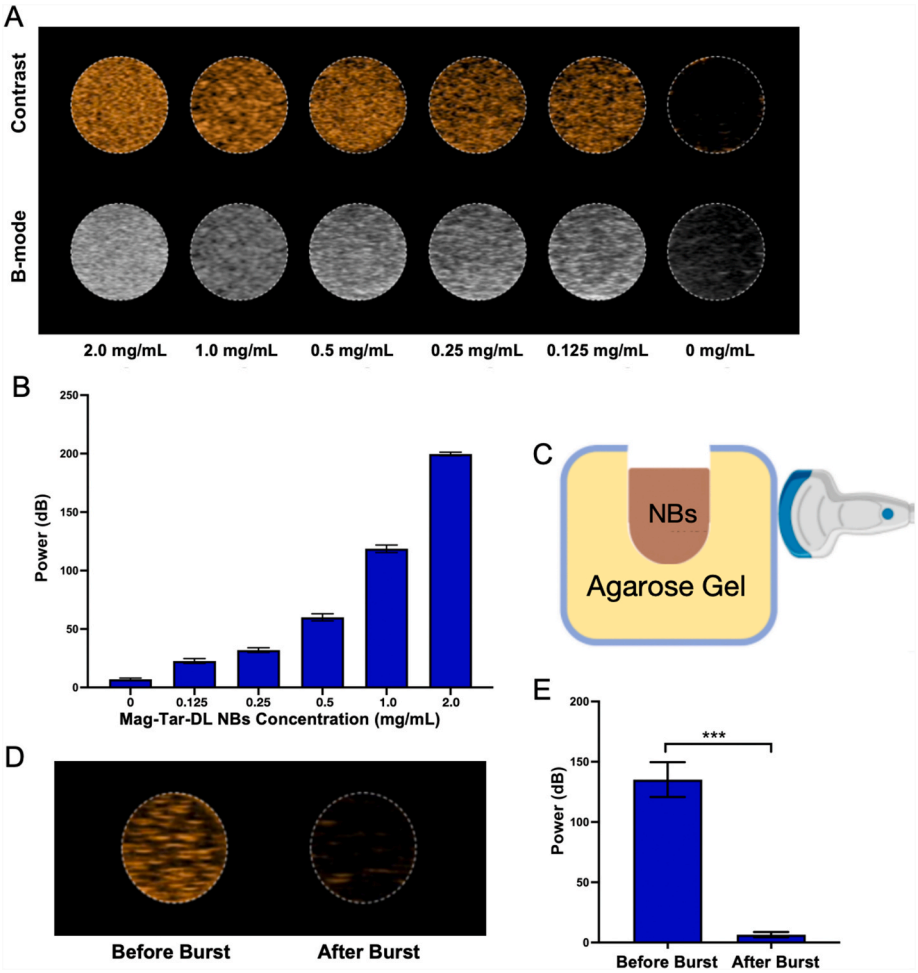

Fig. 3. Acoustic imaging performance and blasting performance of Mag-Tar-DL NBs. (A) The acoustic imaging under the B mode and contrast mode of Mag-Tar-DL NBs *in vitro*. (B) Quantitative analysis of the acoustic imaging performance of Mag-Tar-DL NBs. (C) Schematic diagram of US imaging *in vitro*. (D) The *in vitro* acoustic blasting performance of Mag-Tar-DL NBs. (E) Quantitative analysis of the blasting performance of Mag-Tar-DL NBs (before and after). (***$p < 0.001$).

producing NBs offers advantages such as controllable uniform particle size. PLGA is a polymeric agent that can be metabolized in the human body and the final decomposition products are water and carbon dioxide [25]. Therefore, PLGA possesses high biological safety and be widely used as drug delivery carriers *in vivo* [26–28].

In this study, we constructed Mag-Tar-DL NBs based on PLGA through the water/oil/water system, with dichloromethane as the oil phase for dissolving raw materials including PLGA, Fe_3O_4 nanoparticles, biotin-DSPE-PEG_{2000} and R406. Ammonium bicarbonate was used as a gas-generating agent to be dissolved in the internal phase water, while polyvinyl alcohol (PVA) aqueous solution served as the external aqueous phase to stabilize NBs. Through this system, we successfully produced stable biotin-Mag-DL NBs. During the first emulsification, ammonium bicarbonate solution was encapsulated within the oil phase as the core of the water phase. During the second emulsification, the oil phase with ammonium bicarbonate kernel was dispersed in the PVA solution. After two emulsification steps and organic solvent volatilization, the PLGA, Fe_3O_4, biotin-DSPE-PEG_{2000} and R406 in the oil phase formed the shell structure of NBs [27].

Surface modification of the NBs was achieved through the biotin-avidin bridging method. Avidin, also known as ovalbumin, consists of four identical subunits to form a tetramer and each avidin subunit combines with the Ureido ring in biotin through the tryptophan residue in its structure. Therefore, one avidin molecule has four binding sites with biotin molecule and its binding constant (Ka) is as high as 1015 mol/L [29]. Through this strategy, the VCAM-1 targeting antibody can be efficiently connected to the surface of NBs. To determine the biotin content on the surface of biotin-Mag-TDL NBs, a colorimetric reaction using 3, 3′, 5, 5′-tetramethylbenzidine (TMB) and horseradish peroxidase (HRP) was employed (Fig. S1A). In our study, the excessive HRP-SA binds to biotin-Mag-DL NBs to form HRP labeled SA-Mag-DL NBs. After color reaction with TMB, the absorbance of HRP labeled SA-Mag-DL NBs at 450 nm was substituted into the fitting curve of HRP-SA concentrations and 450 nm absorbance (Fig. S1B). The HRP-SA content on surface of HRP labeled SA-Mag-DL NBs was calculated. Subsequently, the biotin content on surface of biotin-Mag-DL NBs was calculated from HRP-SA content. Finally, it was calculated that the surface of 1 mg of biotinylated NBs can bind 8×10^{-3} μg of SA, thus preparing for connecting targeted VCAM-1 antibody. After connecting VCAM-1 antibody by biotin-avidin bridging method, Mag-Tar-DL NBs were prepared by the above methods, heralding desirable acoustic imaging, magnetic responsiveness and targeting adhesion performance.

After freeze-drying, the morphology of biotin-Mag-DL NBs was observed by scanning electron microscope (SEM), revealing their spherical morphology (Fig. 2A). The result of dynamic light scattering (DLS) exhibited that their hydrodynamic size is around 300–800 nm with an average particle size of approximately 298 nm (Fig. S1C). After synthesizing Mag-Tar-DL NBs, the continuous 7-day DLS test was conducted on the sample. The result showed that the size of the Mag-Tar-DL NBs has not changed significantly (Fig. S1D). As observed from the transmission electron microscope (TEM) image shown in Fig. 2B, the Mag-Tar-DL NBs show a hollow sphere-like structure with the darker

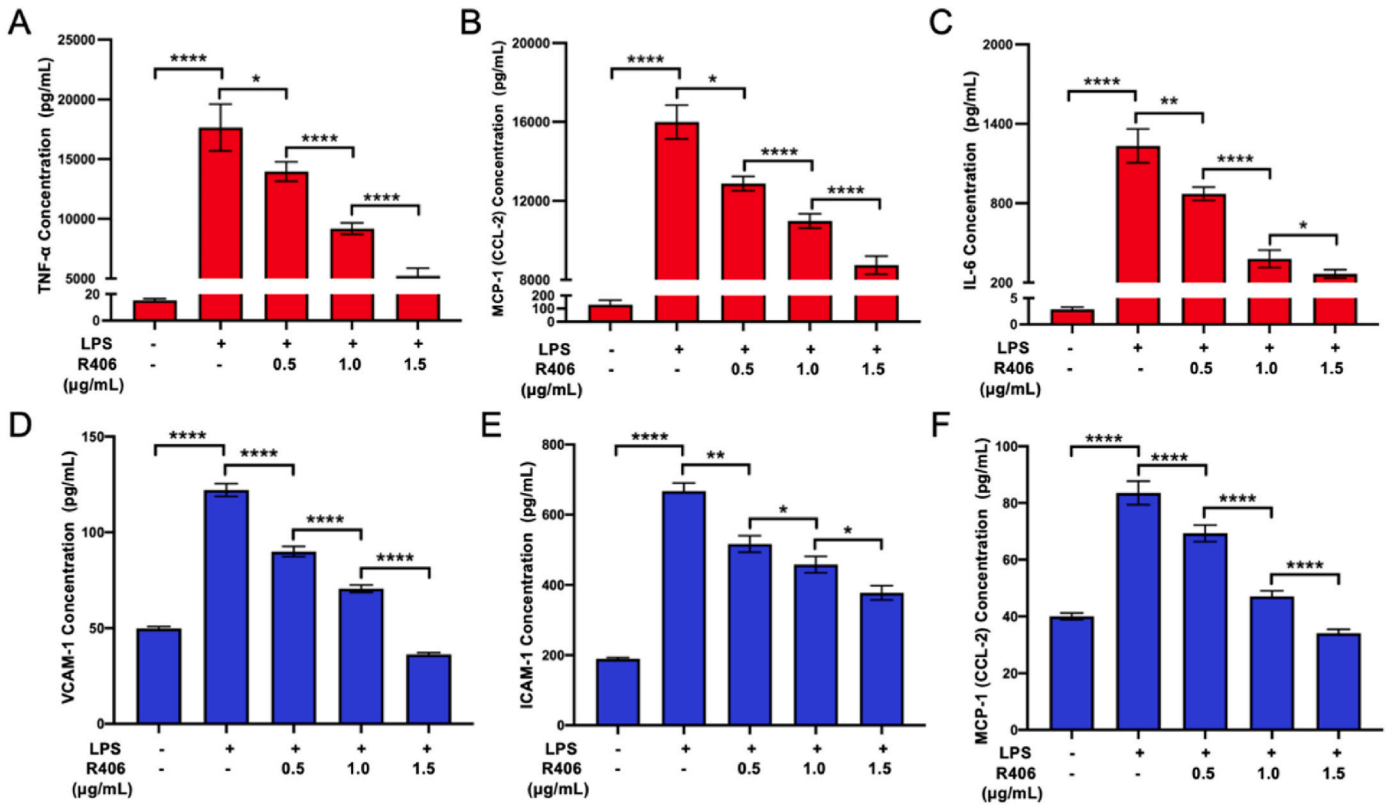

Fig. 4. The inhibition efficiency of R406 on the inflammatory factors' secretion. The inflammatory factors secreted by RAW264.7 macrophage mainly include (A) TNF-α, (B) MCP-1 (CCL-2) and (C) IL-6. The inflammatory factors secreted by HUVEC mainly include (D) VCAM-1, (E) ICAM-1 and (F) MCP-1 (CCL-2). Data are presented as mean ± SD. (*$p < 0.05$, **$p < 0.01$, ***$p < 0.001$ and ****$p < 0.0001$).

Fe_3O_4 nanoparticles were inlaid on the shell of NBs, endowing the NBs with magnetic targeting ability (Fig. 2C). Energy dispersive spectrometer (EDS) elemental mapping analysis further verified the presence of Fe, O, and C elements in the prepared NBs (Fig. 2D). Furthermore, the successful modification of the VCAM-1 antibody on the surface of the Mag-Tar-DL NBs could be evidenced by the confocal laser microscope (CLSM). The merged CLSM image showed co-localization of the red fluorescence emitted by the Dil-labeled NBs and the green fluorescence emitted by the AF488-labeled VCAM-1 antibody, indicating that efficient modification of the biotin-Mag-DL NBs with the VCAM-1 antibody *via* the biotin-avidin bridging method (Fig. 2E). For further confirming the magnetic-targeting behavior of the Mag-Tar-DL NBs, a rubidium magnet was placed on one side of the sample bottle to provide a magnetic field. After 4 min, the magnetic NBs loaded with Fe_3O_4 nanoparticles gathered to the one side of the sample bottle, confirming their favorable magnetic-targeting performance (Fig. 2F).

3.2. R406 loading rate and encapsulation rate

R406, a SYK inhibitor, can reduce the inflammatory response of the vascular endothelium, which can further alleviate the symptom of atherosclerosis [30]. In this study, R406 was used as anti-atherosclerosis drug which was loaded in the Mag-Tar-DL NBs. To confirm the loading rate of R406, the UV–Vis spectroscopy was applied to detect the absorbance of R406 in DMSO solutions with different concentrations. The results indicated that R406 has two characteristic absorption peaks in the wavelength range of 265–400 nm and the absorbance is proportional to the concentration of R406 (Fig. S1E). To verify the successful R406 loading, the R406-loaded NBs were dissolved in DMSO and then detected by UV–Vis spectroscopy. The absorption curve of the R406-loaded NBs sample exhibited similarity to that of pure R406 in the wavelength range of 265–400 nm, indicating that R406 has been successfully loaded into PLGA NBs *via* the double emulsion method. Based on absorbance value of R406-loaded NBs at 280 nm and fitting curve between R406 concentration and 280 nm absorbance value (Fig. S1F), we calculated the encapsulation rate of R406 in DL NBs to be 96.67% and the loading rate of R406 in DL NBs to be 3.87%.

3.3. Contrast-enhanced US imaging of Mag-Tar-DL NBs in vitro

Contrast-enhanced US imaging utilizes hollow sphere-like structures such as microbubbles and NBs to generate nonlinear harmonic signals [31]. Compared to ordinary two-dimensional US imaging, contrast imaging of NBs offers natural advantages. Contrast imaging can distinguish targeted tissue from the background signal of the tissues, thereby improving the sensitivity and specificity of US diagnosis. Agarose gel phantom, which has good sound transmission properties, was used to simulate human tissue. When different concentrations of Mag-Tar-DL NBs dispersion liquid were added to the holes of the agarose gel phantom, the uniform US signal echo can be observed in B mode and Contrast mode by US imaging device (Fig. 3C). The acoustic intensity in the hole increased with the increasing of the Mag-Tar-DL NBs concentration while no significant acoustic signal was detected in the hole of the blank control group (Fig. 3A and B). It demonstrated the excellent contrast-enhanced US imaging ability of Mag-Tar-DL NBs.

3.4. Ultrasonic blasting and release enhancement of R406 by ultrasonic blasting from designed NBs

Ultrasound Targeting Microbubble Destruction (UTMD) is an emerging technology for the controlled release of drugs, playing a significant role in US diagnostics and therapy. UTMD enables US-triggered targeting drug release, thereby increasing cellular uptake and bioavailability of drugs [21,32,33]. Herein, based on the successful

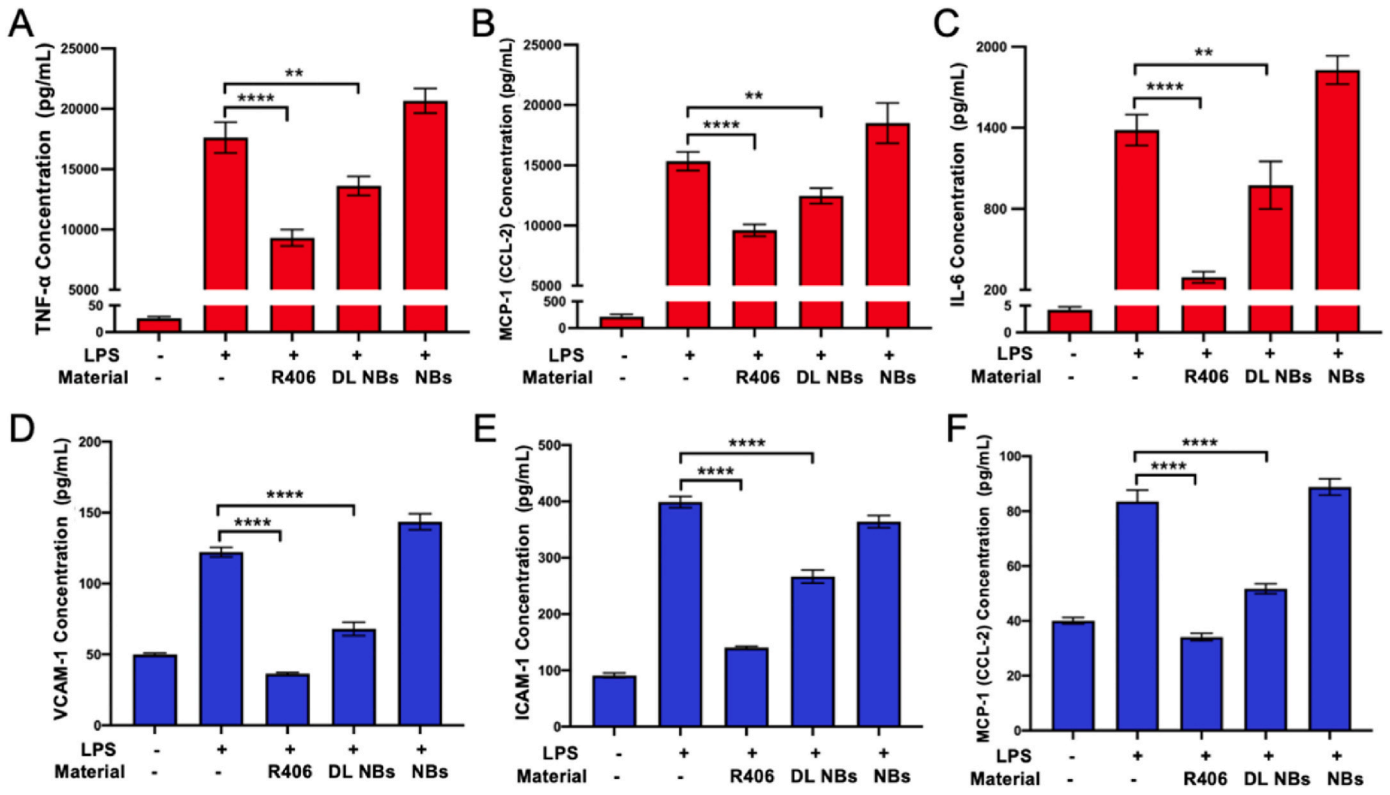

Fig. 5. The inhibition efficiency of R406, R406-loaded NBs and NBs on the inflammatory factors secretion and the ELISA was used to detect the inflammatory factors. The inflammatory factors secreted by RAW264.7 macrophage mainly include (A) TNF-α, (B) MCP-1 (CCL-2) and (C) IL-6. The inflammatory factors secreted by HUVEC mainly include (D) VCAM-1, (E) ICAM-1 and (F) MCP-1 (CCL-2). Data are presented as mean ± SEM. (*$p < 0.05$, **$p < 0.01$, ***$p < 0.001$ and ****$p < 0.0001$).

R406-loading and the dual-targeting behavior, the UTMD was further used to trigger the rapid release of R406 at the atherosclerosis site, enhancing the cellular uptake of R406 and improving the efficiency of atherosclerosis treatment *via* multiple ways: (1) After the effective enrichment in atherosclerosis site based on the dual-targeting effect, the NBs can be crushed by ultrasonic waves to release the loaded R406 controllably *in situ*. (2) Under the influence of US, the NBs can induce a cavitation effect, creating repairable micro gaps in nearby cells. (3) The micro-acoustic flow, shock waves, and blood micro-jets generated during the ultrasonic irradiation of the NBs can increase the uptake of the released R406 in the target tissue [34].

To confirm the US-triggered NBs destruction, 1 mg/mL Mag-Tar-DL NBs was added in the hole of the agarose gel phantom, and the ultrasonic therapy instrument (1 W/cm^2, 50% duty cycle, 1 min) was used to irradiate the Mag-Tar-DL NBs in the hole. After the irradiation, the US imaging device was employed to capture the acoustic imaging of the suspension in the hole. The results showed that the acoustic signal of the NBs in the hole cannot be observed in the US contrast mode after high-power US irradiation (Fig. 3D and E). This suggested that the hollow-like structure of the NBs had been destroyed and cracked to release the loaded R406.

Furthermore, the release of R406 from designed NBs under US irradiation was investigated as well. R406-loaded Mag-Tar-DL NBs was exposed to 1 min of US irradiation at 0 h, 3 h, 6 h and 12 h after initial detection of R406 concentration. The release efficiency increases by 15.1%, 27.2%, 37.1% and 25.8% at 3 h, 6 h, 12h and 24h respectively compared to the group without US blasting. The results showed the release by US excitation plateaued at 12 h, reaching 77 % of the total loading amount at 12 h, significantly higher than that observed without US irradiation, suggesting that the US irradiation can promote the loaded drug released from the designed NBs (Fig. S2).

3.5. *In vitro biosafety evaluation*

To evaluate the biosafety of R406 and the synthesized NBs *in vitro*, RAW264.7 macrophages and HUVEC were incubated with R406 and Mag-Tar-DL NBs for 24 and 48 h. Cell viability was assessed through CCK-8 method. The results demonstrated that within the range of 2.0 μg/mL R406 and 200 μg/mL the designed NBs, as the concentration of drugs and NBs increased, the cell viability of RAW264.7 and HUVEC did not decrease significantly (Figs. S3 and S4), indicating that R406 and the Mag-Tar-DL NBs exhibit insignificant cytotoxicity towards RAW264.7 and HUVEC cells.

3.6. *Anti-inflammatory effect of R406*

R406, a small molecule inhibitor, can inhibit phosphorylation of SYK substrate linker, block activation the SYK dependent immune cell, and reduce immune inflammation mediated by immune complexes [14]. Therefore, R406 can inhibit the expression of inflammatory factors by interrupting the signal transmission of SYK. LPS, a component of the gram-negative bacterial wall, is commonly used to induce cellular inflammation *in vitro*. It stimulates cells into an inflammatory state and secrete various inflammatory factors including TNF-α, MCP-1 (CCL-2), and IL-6 *in vitro* [35,36]. As a pro-inflammatory cytokine, TNF-α can continuously stimulate macrophages in the bloodstream, promotes a 'positive feedback' loop in the inflammatory response, and amplifies inflammation. MCP-1 (CCL-2) is a chemokine that recruits immune cells to sites of inflammation, thus facilitating the spread of the inflammatory response throughout the body [37].

In order to study the inhibition efficiency of R406 and R406-loaded NBs on cell's inflammation, RAW264.7 and HUVEC cells were selected as the research objects. LPS was used to stimulate RAW264.7 and HUVEC cells into the inflammatory state. After co-cultured with R406,

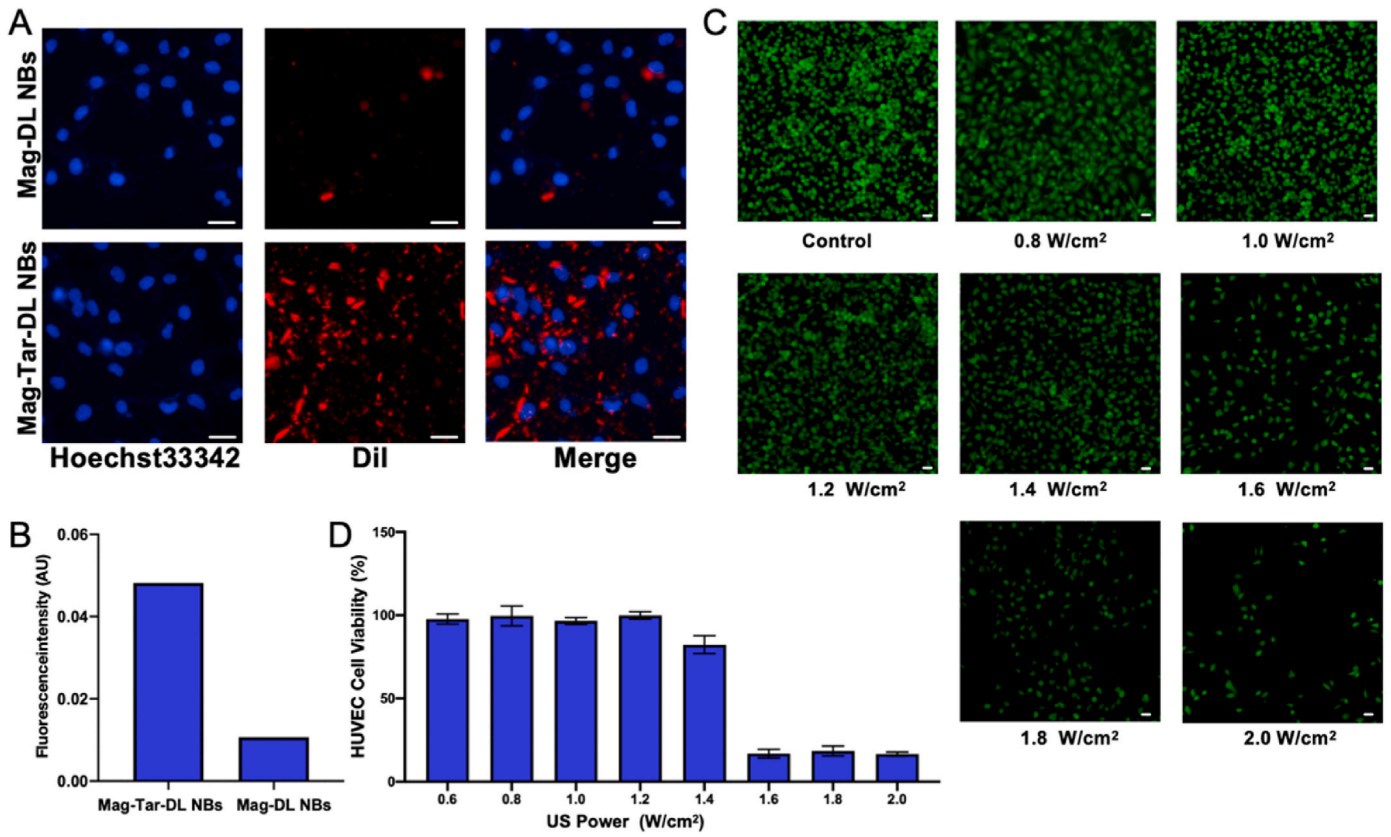

Fig. 6. The antibody targeting adhesion performance of Mag-Tar-DL NBs and Mag-DL NBs *in vitro* and the selection of ultrasonic safety power range. (A) Adherence of Mag-Tar-DL NBs (Dil) and Mag-DL NBs (Dil) on inflammation HUVEC (Hoechst 33342). (B) Quantitative analysis adhesion performance of Mag-Tar-DL NBs and Mag-DL NBs. (C, D) The results of HUVEC's calcein staining and CCK-8 test under the irradiation of different ultrasonic powers (Scale = 50 μm).

ELISA was used to detect the secretion of inflammatory factors in the cell supernatant. The results revealed that R406 can reduce the inflammation generated by both RAW264.7 (Fig. 4A–C) and HUVEC cells (Fig. 4D–F). In the RAW264.7 inflammation system, TNF-α, MCP-1 (CCL-2), and IL6 were selected as detection indicators. In the HUVEC inflammation system, VCAM-1, ICAM-1 and MCP-1 (CCL-2) were selected as the detection indicators. The fitting curve was constructed for different indicators based on the concentrations and 450 nm absorbance values of the standard samples. This allowed us to calculate the secretion of various inflammatory factors in the cell supernatant according to the standard curve, demonstrating a significant inhibitory effect of R406 on inflammation in both macrophages and endothelial cells. Notably, the degree of inhibition was found to be dependent on the concentration of R406, indicating its potential efficacy in treating inflammation-related diseases. As mentioned earlier, R406 achieves its anti-inflammatory effects by inhibiting the SYK pathway, thereby effectively mitigating inflammation in vascular endothelium and blood macrophages, thus presenting a promising therapeutic strategy for atherosclerosis treatment.

3.7. Anti-inflammatory effect of Mag-Tar-DL NBs

In order to study whether R406 retains its anti-inflammation effect when it was encapsulated into PLGA NBs. Free R406, empty NBs and R406-loaded NBs were separately co-cultured with LPS-stimulated RAW264.7 and HUVEC cells. After the co-culture, ELISA was used to detect the secretion of inflammatory factors in the cell supernatant. Results showed that the empty NBs have no obvious effect on inhibiting inflammation. However, both R406 and the R406-loaded NBs significantly inhibited the secretion of inflammatory factors like TNF-α, MCP-1 (CCL-2), IL-6, VCAM-1 and ICAM-1. Noticeably, it indicated that free R406 exhibits a more potent anti-inflammatory effect compared to R406-loaded NBs. This could be due to the slower release kinetics associated with the R406-loaded NBs. In this regard, US-triggered NBs destruction can induce the rapid release of R406 and overcome this limitation. In general, the therapeutic effect of R406 was retained in NBs (Fig. 5).

3.8. Adhesion effect of targeting NBs in vitro

The endothelia cells express various adhesion factors and inflammatory factors in response to mechanical or chemical stimulation. In addition to secreting various inflammatory factors into the blood, the cell surface also expresses various adhesion molecules including VCAM-1 and ICAM-1 which provide the physiological basis for the enrichment of targeting nanoparticles in the targeting area of blood vessels. Aiming at these adhesion molecule receptors, we modified the targeting VCAM-1 molecular probes on the surface of NBs to endow them with the ability to enrich in specific areas. In order to study the adhesion effect of Mag-Tar-DL NBs *in vitro*, LPS was used to stimulate HUVEC into the inflammatory state. The Mag-Tar-DL NBs and Mag-DL NBs were separately incubated with inflammatory HUVEC for 10 min. The unbound NBs was washed away after the incubation with phosphate buffer solution (PBS). In order to observe the adhesion effect, the Hoechst 33342 was used to stain the cell nucleus and Dil was used to label the NBs. Under the fluorescence microscope, we observed a large number of red Mag-Tar-DL NBs adhered to the blue cells while the Mag-DL NBs rarely adhered to HUVEC's surface. It demonstrated the efficient antibody-targeting ability of the Mag-Tar-DL NBs (Fig. 6A and B).

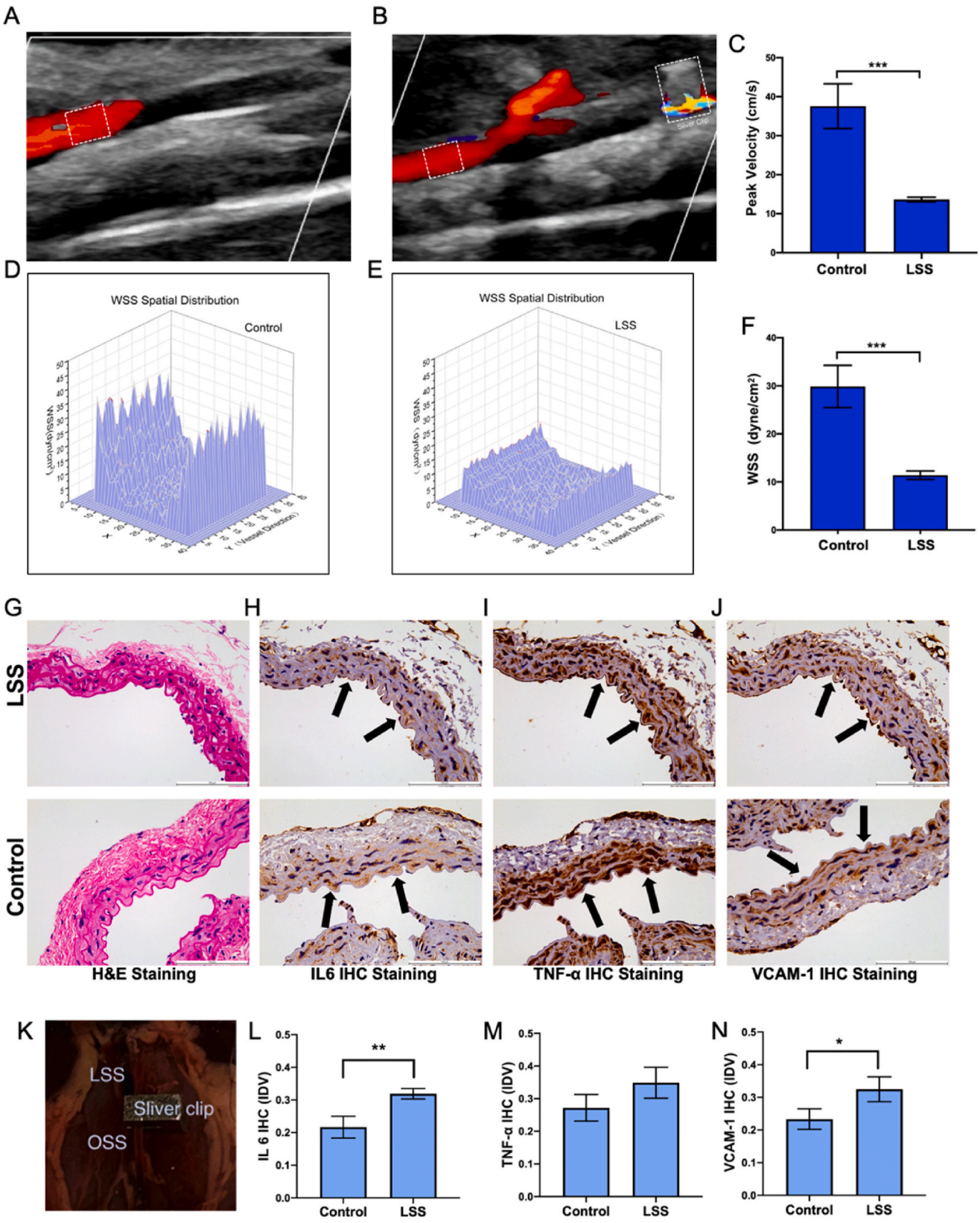

Fig. 7. The US imaging and IHC staining of the LSS area of abdominal aortic in control group and LSS group. Blood flow velocity of (A) control group mice and (B) LSS group mice and (C) their quantification of blood flow velocity. (D–F) WSS analysis and quantification of control group mice and LSS group mice. (G–J) H&E staining and IHC staining (IL-6, TNF-α and VCAM-1) of control group mice and LSS group mice (K) Modeling indication. (L-N). the quantification of IHC including IL-6, TNF-α and VCAM-1 (Scale = 100 μm). Data are presented as mean ± SEM. (*$p < 0.05$, **$p < 0.01$ and ***$p < 0.001$).

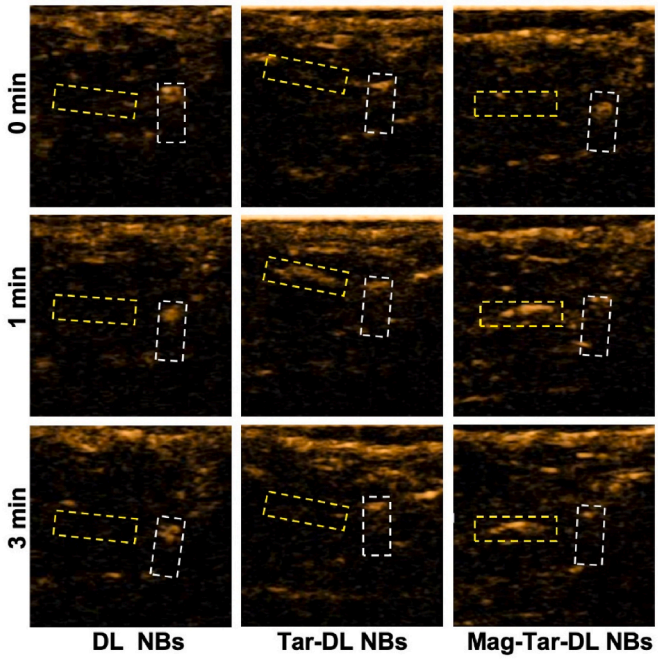

Fig. 8. The *in vivo* US contrast images of LSS area at different time points (0, 1 and 3 min) after injection of DL NBs, Tar-DL NBs, and Mag-Tar-DL NBs. The yellow dashed box indicates the aorta, and the white dashed box indicates the silver clip.

3.9. Selection of safe US power density

While increasing the US irradiation energy can facilitate the lysis of the NBs and the release of the encapsulated drug, it is crucial to acknowledge that a higher ultrasonic intensity does not automatically ensure improved therapeutic outcomes. Excessive US irradiation can damage the vascular endothelium, emphasizing the need to carefully select the appropriate ultrasonic irradiation parameters for *in vivo* experiments. To achieve this goal, we conducted simulations of US irradiation on endothelial cells *in vitro*. The calcein-staining and CCK-8 method were utilized to analyze the activity of HUVEC following US irradiation at different power levels (Fig. 6C and D). Based on the CLSM observations and CCK-8 assay results, it has been determined that ultrasonic irradiation does not significantly impact the cell viability of HUVEC at powers lower than 1.2 W/cm^2. When the ultrasonic irradiation power is higher than 1.4 W/cm^2, the cell viability began to decrease significantly. Therefore, US power within 1.2 W/cm^2 was selected for the further experiments *in vivo* to realize the US triggered treatment and the biosafety of endothelial cells.

3.10. Enhancement of drug therapeutic effects by US

Previous studies have demonstrated that US can facilitate the cellular uptake of drugs through various biological effects, such as cavitation, thereby augmenting their therapeutic efficacy [38]. In this study, HUVEC was exposed to US, and MCP-1 (CCL-2) was selected as the typical detection indicator to explore the potential enhancement of the anti-inflammatory effect of R406 under US irradiation. Our findings revealed that the expression of MCP-1 (CCL-2) in the R406+US group was lower than the R406 group, indicating a stronger anti-inflammatory effect of R406 when combined with US irradiation (Fig. S5). It suggested that US has the capability to enhance the therapeutic effects of drugs.

3.11. LSS model

WSS is the tangential friction force of the blood flowing in the blood vessel against the blood vessel wall. Vascular endothelial cells can sense the changes in blood flow shear stress, which is widely regarded as the most significant mechanical factor contributing to atherosclerosis and plaque rupture [39]. Studies showed that abnormal blood flow morphology such as the decreasing WSS, non-laminar flow, turbulent flow, may be related to the pathological changes of atherosclerosis [38]. In recent years, many experiments *in vitro* supported the view of LSS can induce atherosclerosis [5,40]. Continuously decreasing WSS can stimulate the thickening of the arterial intima and the proliferation of media smooth muscle, suggesting that a reduction in WSS is one of the factors contributing to atherosclerosis development [41,42]. Caroline Cheng et al. have demonstrated that LSS can readily induce atherosclerosis by creating a model of localized stenosis in the common carotid artery and plaques caused by LSS have a larger lesion and more vulnerable plaque phenotype [43].

There are various methods to establish LSS model including surgical thread ligation, chemical burn method and balloon injury protocol [44,45]. In this study, an arterial silver clip with an inner diameter of 0.2 mm was utilized to create an LSS model on the abdominal aorta of C57 mice (Fig. 7K, Fig. S6). Compared with other methods, the arterial silver clip can create an arterial injury model with the same stenosis size and eliminate the difference in stenosis size caused by surgical error [11]. After anesthetizing the mice with sodium pentobarbital, we opened the abdominal cavity and separated the abdominal aorta. The 0.2 mm arterial silver clip was placed on the abdominal aorta. After establishing the LSS model, the blood flow velocity and WSS in the abdominal aorta of both the control group mice and the model group mice were measured using the US imager (Fig. 7A–F). The results displayed that the blood flow velocity of the abdominal aorta was significantly reduced in the model group mice compared with the control mice (Fig. 7A–C) and the WSS in the LSS area in front of the artery stenosis was also significantly reduced (Fig. 7D–F). It showed the success of the surgical model. To confirm the effect of LSS, we took out the abdominal aorta from model group mice and normal mice in the fourteenth day after modeling and prepared them into paraffin sections. H&E staining and IHC staining were performed on the paraffin sections (Fig. 7G–J). The IHC staining results in LSS group showed that, the staining amount at the endothelial cells in the LSS areas is relatively deep (indicated by arrows), it indicated that endothelial cells expressed a large number of inflammatory factors (IL-6 and TNF-α) and adhesion molecules (VCAM-1) under the influence of LSS. In the control group, the IHC staining amount at the endothelial cells was not deep as the LSS group (Fig. 7H–J). The results of quantitative analysis showed the vascular endothelial cells under the influence of LSS expressed more inflammatory factors (IL-6) and adhesion molecules (VCAM-1) indeed (Fig. 7L-N). It indicated that LSS can stimulate vascular endothelial into inflammation and up-regulate the secretion of endothelial cell inflammatory factors and adhesion molecules.

3.12. US imaging of Mag-Tar-DL NBs in vivo

In order to study the adhesion of Mag-Tar-DL NBs in LSS areas, we separately injected DL NBs, Tar-DL NBs and Mag-Tar-DL NBs into the LSS model mice through tail vein way. The dose of injected NBs is 0.5 mg/kg. In Fig. 8, the white dashed box corresponds to the silver clip, and the yellow dashed box represents the LSS area situated behind the silver clip. Within the DL NBs group, it is evident that DL NBs transiently traverse the LSS region within 1 min, exhibiting minimal adhesion to this area. Conversely, Tar-DL NBs pass through the LSS region and demonstrate a certain degree of adherence attributable to the antibody targeting effect. After 1 min of injection, the echo of Tar-DL NBs can still be observed in the LSS region. Subsequently, over a 3-min period, the number of Tar-DL NBs adhering to the LSS area gradually diminishes and eventually disappears due to the continuous influence of blood flow. In the Mag-Tar-DL NBs group, due to the combined effect of antibody targeting and magnetic targeting, a substantial number of NBs can be observed within the LSS region within 1 min of injection. Despite the

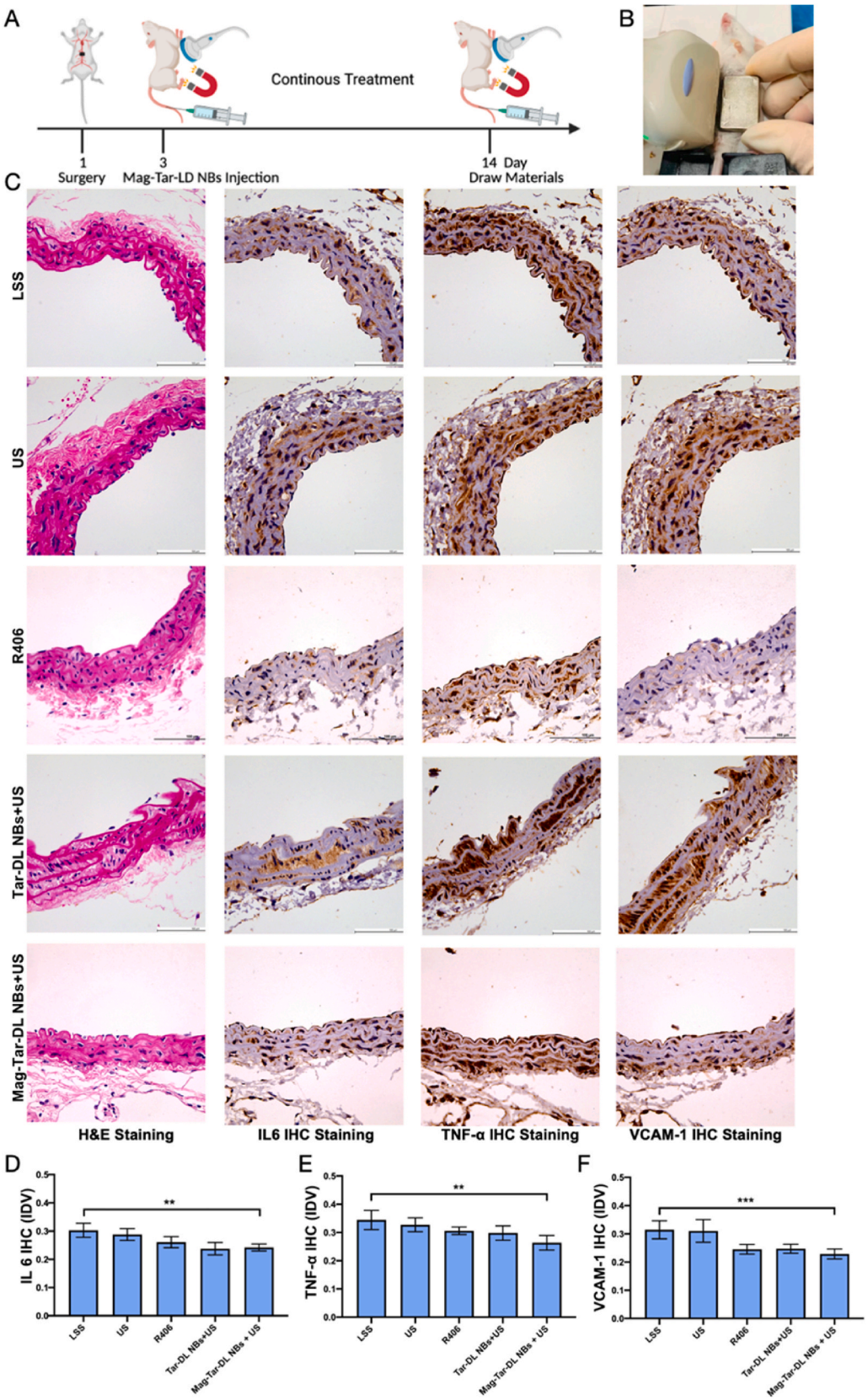

Fig. 9. The therapeutic effect of Mag-Tar-DL NBs *in vivo*. (A) The treatment process of Mag-Tar-DL NBs *in vivo*. (B) Experimental image of Mag-Tar-DL NBs with US and magnet *in vivo*. (C) Histological analysis of the abdominal aorta was evaluated *via* H&E staining and IHC staining. (D, E, F) Quantitative IHC (IL6, TNF-α and VCAM-1) analysis of arterial endothelium. (Scale = 100 μm). Data are presented as mean ± SEM. (*$p < 0.05$, **$p < 0.01$ and ***$p < 0.001$).

continuous impact of blood flow, Mag-Tar-DL NBs can continue to remain in the LSS region under the magnetic targeting force. Even after 3 min of injection, Mag-Tar-DL NBs that remain within the LSS region due to the magnetic field.

3.13. Treatment effect of Mag-Tar-DL NBs in vivo

To study the therapeutic effect of Mag-Tar-DL NBs, the mice were divided into 5 groups randomly after batch modeling (Control group, US group, R406 group, Tar-DL NBs + US group, Mag-Tar-DL NBs + US group) (Fig. S7). The treatment started from the third day after the successful modeling (Fig. 9A and B). The same as the R406 group, both the Tar-DL NBs and Mag-Tar-DL NBs were administered with the same R406 dose of 5 mg/kg. After consecutive 12-day treatment, the abdominal aorta of LSS area was taken out, paraffin-embedded and sectioned. H&E staining and IHC staining were performed. The staining results showed that compared to the LSS group, there was no significant decrease in the expression of inflammatory factors on the endothelial surface in the US group. In addition, the expression levels of inflammatory factors in endothelial cells of other treatment groups showed a decreasing trend to varying degrees (Fig. 9C). Image J software was used to quantitatively analyze the inflammatory factors on the endothelium. The results showed that LSS can induce the endothelium of the abdominal aorta of mice to express a large number of inflammatory mediators and adhesion factors. Under normal circumstances, monocytes, white blood cells and platelets in the blood hardly adhere to the vascular endothelium. Under the stimulation of LSS, the endothelium begins to express a large number of inflammatory mediators and adhesion factors such as VCAM-1 and ICAM-1. Monocytes are more likely to adhere to the vascular endothelium, invade the vascular intima and evolve into foam cells. Under the action of long-term LSS, local vascular inflammation can easily develop into atherosclerotic plaque [40]. Therefore, Effective delivery of R406, a SYK inhibitor, can significantly impede the progression of atherosclerosis. Through the combined application of magnetic and antibody targeting, Mag-Tar-DL NBs accumulate and release R406 within areas of LSS, optimizing therapeutic impact. The IHC staining results showed that, in Mag-Tar-DL NBs + US group, the expression of TNF-α, IL-6 and VCAM-1 in the vascular endothelium was significantly lower than LSS group. In addition, through analyzing the IHC staining results of other therapeutic groups, we found that in the other therapeutic groups containing R406, the inflammatory factors in the LSS region showed varying degrees of decrease. In the IL-6 and VCAM-1 IHC staining results, Mag-Tar-DL NBs + US group showed little difference in treatment efficacy compared to other treatments. In the IHC staining results of TNF-α, among the groups, the therapeutic effect of Mag-Tar-DL NBs was the best. The cause of this situation may be due to the short treatment cycle, and the difference in treatment effectiveness is not very significant. However, the results still show a good downward trend. It indicated the potential application of Mag-Tar-DL NBs in anti-atherosclerosis (Fig. 9D–F).

4. Conclusion

In summary, this study has successfully developed Mag-Tar-DL NBs utilizing the double emulsion method and the biotin-avidin bridging technique. These NBs have exhibited excellent characteristics, including magnetic responsiveness, targeted antibody delivery, biocompatibility, anti-inflammatory effects, and US imaging capabilities in both *in vitro* and *in vivo* settings. Abnormal hemodynamics such as LSS can provoke an inflammatory response in the arterial intima and lead to atherosclerosis. To address this issue, we utilized a surgical technique to construct the LSS model and deployed Mag-Tar-DL NBs with dual targeting effects to deliver R406 to the LSS area. Subsequently, UTMD was employed to facilitate the rapid *in situ* release of R406 from the Mag-Tar-DL NBs to inhibit inflammation in the LSS area. As expected, guided by an external magnetic field and targeted antibodies, Mag-Tar-DL NBs accumulated in the LSS area and inhibited inflammation, thereby preventing the progression of atherosclerosis. Importantly, this study provides a controllable drug delivery system under US imaging guidance, which improves the efficiency of anti-atherosclerosis therapy and offers a promising new method for drug delivery in large and medium arteries.

CRediT authorship contribution statement

Jie Lin: Writing – review & editing, Writing – original draft, Visualization, Validation, Software, Resources, Project administration, Methodology, Investigation, Formal analysis, Data curation. **Xiaoying Chen:** Writing – review & editing, Writing – original draft, Visualization, Validation, Software, Resources, Project administration, Methodology, Investigation, Formal analysis, Data curation. **Yi Li:** Writing – review & editing, Writing – original draft, Visualization, Validation, Software, Resources, Investigation, Formal analysis, Data curation. **Luodan Yu:** Writing – review & editing, Writing – original draft, Visualization, Validation, Supervision, Software, Resources, Project administration, Methodology, Investigation, Funding acquisition, Formal analysis, Data curation, Conceptualization. **Yu Chen:** Writing – review & editing, Writing – original draft, Visualization, Validation, Supervision, Software, Resources, Project administration, Methodology, Investigation, Funding acquisition, Formal analysis, Data curation, Conceptualization. **Bo Zhang:** Writing – review & editing, Writing – original draft, Visualization, Validation, Supervision, Software, Resources, Project administration, Methodology, Investigation, Funding acquisition, Formal analysis, Data curation, Conceptualization.

Declaration of competing interest

The authors declare that they have no known competing financial interests or personal relationships that could have appeared to influence the work reported in this paper.

Data availability

Data will be made available on request.

Acknowledgement

The work was funded by the Major projects of the National Natural Science Foundation of China (Grant No. 82371988, 82171950, 81871361, 32271457), and Important Weak Subject Construction Project of Shanghai Pudong New Area Health Commission (Grant No. PWZbr2022-12).

Appendix A. Supplementary data

Supplementary data to this article can be found online at https://doi.org/10.1016/j.mtbio.2024.101037.

References

[1] W. Herrington, B. Lacey, P. Sherliker, J. Armitage, S. Lewington, Epidemiology of atherosclerosis and the potential to reduce the global burden of atherothrombotic disease, Circ. Res. 118 (4) (2016) 535–546, https://doi.org/10.1161/circresaha.115.307611.

[2] B. Lavin Plaza, A. Phinikaridou, M.E. Andia, M. Potter, S. Lorrio, I. Rashid, R. M. Botnar, Sustained focal vascular inflammation accelerates atherosclerosis in remote arteries, Arterioscler. Thromb. Vasc. Biol. 40 (9) (2020) 2159–2170, https://doi.org/10.1161/atvbaha.120.314387.

[3] E. Falk, Pathogenesis of atherosclerosis, J. Am. Coll. Cardiol. 47 (8 Suppl) (2006) C7–C12, https://doi.org/10.1016/j.jacc.2005.09.068.

[4] H. Samady, D.S. Molony, A.U. Coskun, A.S. Varshney, B. De Bruyne, P.H. Stone, Risk stratification of coronary plaques using physiologic characteristics by CCTA: Focus on shear stress, J Cardiovasc Comput Tomogr 14 (5) (2020) 386–393, https://doi.org/10.1016/j.jcct.2019.11.012.

[5] Z. Teng, S. Wang, A. Tokgoz, V. Taviani, J. Bird, U. Sadat, Y. Huang, A.J. Patterson, N. Figg, M.J. Graves, J.H. Gillard, Study on the association of wall shear stress and vessel structural stress with atherosclerosis: an experimental animal study,

Atherosclerosis 320 (2021) 38–46, https://doi.org/10.1016/j.atherosclerosis.2021.01.017.
[6] J. Malik, L. Novakova, A. Valerianova, E. Chytilova, V. Lejsek, k. Buryskova Salajova, L. Lambert, T. Grus, M. Porizka, P. Michalek, Wall shear stress alteration: a local risk factor of atherosclerosis, Curr Atheroscler Rep 24 (3) (2022) 143–151, https://doi.org/10.1007/s11883-022-00993-0.
[7] S. Lehoux, E.A. Jones, Shear stress, arterial identity and atherosclerosis, Thromb Haemost 115 (3) (2016) 467–473, https://doi.org/10.1160/th15-10-0791.
[8] R. Li, J.G. Zijlstra, J.A. Kamps, M. van Meurs, G. Molema, Abrupt reflow enhances cytokine-induced proinflammatory activation of endothelial cells during simulated shock and resuscitation, Shock 42 (4) (2014) 356–364, https://doi.org/10.1097/shk.0000000000000223.
[9] M. Fukuda, T. Aoki, Molecular basis for intracranial aneurysm formation, Acta Neurochir. Suppl. 120 (2015) 13–15, https://doi.org/10.1007/978-3-319-04981-6_2.
[10] Q. Ren, L. Ren, C. Ren, X. Liu, C. Dong, X. Zhang, Platelet endothelial cell adhesion molecule-1 (PECAM1) plays a critical role in the maintenance of human vascular endothelial barrier function, Cell Biochem. Funct. 33 (8) (2015) 560–565, https://doi.org/10.1002/cbf.3155.
[11] L. Xia, B. Zhang, Y. Sun, B. Chen, Z. Yu, Analysis of syk/pecam-1 signaling pathway in low shear stress induced atherosclerosis based on ultrasound imaging, Comput Methods Programs Biomed 201 (2021) 105953, https://doi.org/10.1016/j.cmpb.2021.105953.
[12] Y.C. Lin, D.Y. Huang, J.S. Wang, Y.L. Lin, S.L. Hsieh, K.C. Huang, W.W. Lin, Syk is involved in NLRP3 inflammasome-mediated caspase-1 activation through adaptor asc phosphorylation and enhanced oligomerization, J. Leukoc. Biol. 97 (5) (2015) 825–835, https://doi.org/10.1189/jlb.3HI0814-371RR.
[13] A. Mócsai, J. Ruland, V.L. Tybulewicz, The syk tyrosine kinase: a crucial player in diverse biological functions, Nat. Rev. Immunol. 10 (6) (2010) 387–402, https://doi.org/10.1038/nri2765.
[14] S. Braselmann, V. Taylor, H. Zhao, S. Wang, C. Sylvain, M. Baluom, K. Qu, E. Herlaar, A. Lau, C. Young, B.R. Wong, S. Lovell, T. Sun, G. Park, A. Argade, S. Jurcevic, P. Pine, R. Singh, E.B. Grossbard, D.G. Payan, E.S. Masuda, R406, an orally available spleen tyrosine kinase inhibitor blocks fc receptor signaling and reduces immune complex-mediated inflammation, J Pharmacol Exp Ther 319 (3) (2006) 998–1008, https://doi.org/10.1124/jpet.106.109058.
[15] X. Su, Z.H. Sun, Q. Ren, J.R. Liu, L. Yin, N. Liang, L. Meng, R.X. Sun, The effect of spleen tyrosine kinase inhibitor R406 on diabetic retinopathy in experimental diabetic rats, Int. Ophthalmol. 40 (9) (2020) 2371–2383, https://doi.org/10.1007/s10792-020-01422-4.
[16] T. Nezu, N. Hosomi, S. Aoki, M. Matsumoto, Carotid intima-media thickness for atherosclerosis, J Atheroscler Thromb 23 (1) (2016) 18–31, https://doi.org/10.5551/jat.31989.
[17] T. Quillard, P. Libby, Molecular imaging of atherosclerosis for improving diagnostic and therapeutic development, Circ. Res. 111 (2) (2012) 231–244, https://doi.org/10.1161/circresaha.112.268144.
[18] J. Baier, A. Rix, F. Kiessling, Molecular ultrasound imaging, recent results, Cancer Res. 216 (2020) 509–531, https://doi.org/10.1007/978-3-030-42618-7_15.
[19] A.F. Schinkel, M. Kaspar, D. Staub, Contrast-enhanced ultrasound: clinical applications in patients with atherosclerosis, Int J Cardiovasc Imaging 32 (1) (2016) 35–48, https://doi.org/10.1007/s10554-015-0713-z.
[20] S. Roovers, T. Segers, G. Lajoinie, J. Deprez, M. Versluis, S.C. De Smedt, I. Lentacker, The role of ultrasound-driven microbubble dynamics in drug delivery: from microbubble fundamentals to clinical translation, Langmuir 35 (31) (2019) 10173–10191, https://doi.org/10.1021/acs.langmuir.8b03779.
[21] J. Sitta, C.M. Howard, Applications of ultrasound-mediated drug delivery and gene therapy, Int. J. Mol. Sci. 22 (21) (2021) 11491, https://doi.org/10.3390/ijms222111491.
[22] J. Wang, Z. Li, M. Pan, M. Fiaz, Y. Hao, Y. Yan, L. Sun, F. Yan, Ultrasound-mediated blood-brain barrier opening: an effective drug delivery system for theranostics of brain diseases, Adv. Drug Deliv. Rev. 190 (2022) 114539, https://doi.org/10.1016/j.addr.2022.114539.
[23] D.W. Kurniawan, A.K. Jajoriya, G. Dhawan, D. Mishra, J. Argemi, R. Bataller, G. Storm, D.P. Mishra, J. Prakash, R. Bansal, Therapeutic inhibition of spleen tyrosine kinase in inflammatory macrophages using PLGA nanoparticles for the treatment of non-alcoholic steatohepatitis, J Control Release 288 (2018) 227–238, https://doi.org/10.1016/j.jconrel.2018.09.004.
[24] S. Ding, C.A. Serra, T.F. Vandamme, W. Yu, N. Anton, Double emulsions prepared by two-step emulsification: History, state-of-the-art and perspective, J Control Release 295 (2019) 31–49, https://doi.org/10.1016/j.jconrel.2018.12.037.
[25] J.M. Lü, X. Wang, C. Marin-Muller, H. Wang, P.H. Lin, Q. Yao, C. Chen, Current advances in research and clinical applications of PLGA-based nanotechnology, Expert Rev. Mol. Diagn 9 (4) (2009) 325–341, https://doi.org/10.1586/erm.09.15.
[26] F. Danhier, E. Ansorena, J.M. Silva, R. Coco, A. Le Breton, V. Préat, PLGA-based nanoparticles: an overview of biomedical applications, J Control Release 161 (2) (2012) 505–522, https://doi.org/10.1016/j.jconrel.2012.01.043.
[27] Y. Chen, Y. Liang, P. Jiang, F. Li, B. Yu, F. Yan, Lipid/PLGA hybrid microbubbles as a versatile platform for noninvasive image-guided targeted drug delivery, ACS Appl. Mater. Interfaces 11 (45) (2019) 41842–41852, https://doi.org/10.1021/acsami.9b10188.
[28] Y. Su, B. Zhang, R. Sun, W. Liu, Q. Zhu, X. Zhang, R. Wang, C. Chen, PLGA-based biodegradable microspheres in drug delivery: recent advances in research and application, Drug Deliv. 28 (1) (2021) 1397–1418, https://doi.org/10.1080/10717544.2021.1938756.
[29] M. Wilchek, E.A. Bayer, Introduction to avidin-biotin technology, Methods Enzymol. 184 (1990) 5–13, https://doi.org/10.1016/0076-6879(90)84256-g.
[30] S.P. McAdoo, M. Prendecki, A. Tanna, T. Bhatt, G. Bhangal, J. McDaid, E. S. Masuda, H.T. Cook, F.W.K. Tam, C.D. Pusey, Spleen tyrosine kinase inhibition is an effective treatment for established vasculitis in a pre-clinical model, Kidney Int. 97 (6) (2020) 1196–1207, https://doi.org/10.1016/j.kint.2019.12.014.
[31] D. Cosgrove, Ultrasound contrast agents: an overview, Eur. J. Radiol. 60 (3) (2006) 324–330, https://doi.org/10.1016/j.ejrad.2006.06.022.
[32] Z.Y. Chen, F. Yang, Y. Lin, J.S. Zhang, R.X. Qiu, L. Jiang, X.X. Zhou, J.X. Yu, New development and application of ultrasound targeted microbubble destruction in gene therapy and drug delivery, Curr. Gene Ther. 13 (4) (2013) 250–274, https://doi.org/10.2174/15665232113139990003.
[33] Y. Wang, X. Li, L. Liu, B. Liu, F. Wang, C. Chen, Tissue targeting and ultrasound-targeted microbubble destruction delivery of plasmid DNA and transfection in vitro, Cell. Mol. Bioeng. 13 (1) (2020) 99–112, https://doi.org/10.1007/s12195-019-00597-w.
[34] X. Zhou, H. Liu, Y. Pang, M. Wang, S. Liu, UTMD-mediated delivery of miR-21-5p inhibitor suppresses the development of lung cancer, Tissue Cell 74 (2022) 101719, https://doi.org/10.1016/j.tice.2021.101719.
[35] H. Ogawa, K. Mukai, Y. Kawano, Y. Minegishi, H. Karasuyama, Th2-inducing cytokines IL-4 and IL-33 synergistically elicit the expression of transmembrane tnf-α on macrophages through the autocrine action of IL-6, Biochem. Biophys. Res. Commun. 420 (1) (2012) 114–118, https://doi.org/10.1016/j.bbrc.2012.02.124.
[36] S.L. Deshmane, S. Kremlev, S. Amini, B.E. Sawaya, Monocyte chemoattractant protein-1 (MCP-1): an overview, J. Interferon Cytokine Res. 29 (6) (2009) 313–326, https://doi.org/10.1089/jir.2008.0027.
[37] K.C. Koskinas, Y.S. Chatzizisis, M.I. Papafaklis, A.U. Coskun, A.B. Baker, P. Jarolim, A. Antoniadis, E.R. Edelman, P.H. Stone, C.L. Feldman, Synergistic effect of local endothelial shear stress and systemic hypercholesterolemia on coronary atherosclerotic plaque progression and composition in pigs, Int. J. Cardiol. 169 (6) (2013) 394–401, https://doi.org/10.1016/j.ijcard.2013.10.021.
[38] K.C. Koskinas, G.K. Sukhova, A.B. Baker, M.I. Papafaklis, Y.S. Chatzizisis, A. U. Coskun, T. Quillard, M. Jonas, C. Maynard, A.P. Antoniadis, G.P. Shi, P. Libby, E.R. Edelman, C.L. Feldman, P.H. Stone, Thin-capped atheromata with reduced collagen content in pigs develop in coronary arterial regions exposed to persistently low endothelial shear stress, Arterioscler. Thromb. Vasc. Biol. 33 (7) (2013) 1494–1504, https://doi.org/10.1161/atvbaha.112.300827.
[39] T.G. Papaioannou, E.N. Karatzis, M. Vavuranakis, J.P. Lekakis, C. Stefanadis, Assessment of vascular wall shear stress and implications for atherosclerotic disease, Int. J. Cardiol. 113 (1) (2006) 12–18, https://doi.org/10.1016/j.ijcard.2006.03.035.
[40] V. Peiffer, S.J. Sherwin, P.D. Weinberg, Does low and oscillatory wall shear stress correlate spatially with early atherosclerosis? A systematic review, Cardiovasc. Res. 99 (2) (2013) 242–250, https://doi.org/10.1093/cvr/cvt044.
[41] C. Zaragoza, S. Márquez, M. Saura, Endothelial mechanosensors of shear stress as regulators of atherogenesis, Curr. Opin. Lipidol. 23 (5) (2012) 446–452, https://doi.org/10.1097/MOL.0b013e328357e837.
[42] M. Hammes, K. Cassel, M. Boghosian, S. Watson, B. Funaki, F. Coe, A cohort study showing correspondence of low wall shear stress and cephalic arch stenosis in brachiocephalic arteriovenous fistula access, J. Vasc. Access (2020) 1129729820942048, https://doi.org/10.1177/1129729820942048, 10.1177/1129729820942048.
[43] C. Cheng, D. Tempel, R. van Haperen, A. van der Baan, F. Grosveld, M.J. Daemen, R. Krams, R. de Crom, Atherosclerotic lesion size and vulnerability are determined by patterns of fluid shear stress, Circulation 113 (23) (2006) 2744–2753, https://doi.org/10.1161/circulationaha.105.590018.
[44] Y. Yu, Z. Cai, M. Cui, P. Nie, Z. Sun, S. Sun, S. Chu, X. Wang, L. Hu, J. Yi, L. Shen, B. He, The orphan nuclear receptor Nur77 inhibits low shear stress-induced carotid artery remodeling in mice, Int. J. Mol. Med. 36 (6) (2015) 1547–1555, https://doi.org/10.3892/ijmm.2015.2375.
[45] Y. Sun, B. Zhang, L. Xia, Effect of low wall shear stress on the morphology of endothelial cells and its evaluation indicators, Comput Methods Programs Biomed 208 (2021) 106082, https://doi.org/10.1016/j.cmpb.2021.106082.